# Regional and Seasonal Trends in Tropical Ozone from SHADOZ Profiles: Reference for Models and Satellite Products

30 Jan 2021

**Anne M. Thompson[1*], Ryan M. Stauffer[1,2], Jacquelyn C. Witte[3], Debra E. Kollonige[1,4], Krzysztof Wargan[1,4], Jerald R. Ziemke[1,5]**

[1]NASA/Goddard Space Flight Center (GSFC), Greenbelt, MD, USA anne.m.thompson@nasa.gov; ORCID: 0000-0002-7829-0920

[2]Earth System Science Interdisciplinary Center, University of Maryland, College Park, MD ryan.m.stauffer@nasa.gov; ORCID: 0000-0002-8583-7795

[3]National Center for Atmospheric Research Earth Observations Laboratory, Boulder, CO jwitte@ucar.edu; ORCID: 0000-0002-4110-5277

[4]Science Systems and Applications, Inc., Lanham, MD, debra.e.kollonige@nasa.gov; ORCID: 0000-0002-6597-328X; krzysztof.wargan-1@nasa.gov; ORCID: 0000-0002-3795-2983

[5]Morgan State Univ., Baltimore, MD, jerald.r.ziemke@nasa.gov; ORCID: 0000-0002-5575-3654

*Corresponding author: Anne M. Thompson (anne.m.thompson@nasa.gov)

**Key Points:**

- Trends in free tropospheric (FT), lowermost stratospheric (LMS) $O_3$, tropopause height and a convective proxy at SHADOZ sites were computed
- FT $O_3$ increases and LMS $O_3$ decreases vary by season and region. Only 1 station shows an annual LMS loss; 2 stations display FT increases
- LMS $O_3$ increases (decreases) occur in low (high)-$O_3$ months, correlated with tropopause height; FT $O_3$ increases most in February to April

**Keywords:** Tropical Ozone Trends, Lower Stratosphere, Ozonesondes, Free Troposphere, SHADOZ

Index Terms: 341, 365, 1620, 3309, 3314

**Abstract.** Understanding trends in lowermost stratosphere (LMS) and free tropospheric (FT) ozone is an important topic in the climate assessment community because of feedbacks among changing temperature, dynamics and ozone. Most LMS evaluations are based on satellite observations. FT ozone assessments rely heavily on profiles from commercial aircraft. Ozonesondes provide an independent profile dataset that encompasses both stratosphere and troposphere. We used v06 Southern Hemisphere Additional Ozonesondes (SHADOZ) data from 1998-2019 in a Multiple Linear Regression model to analyze variability and trends in ozone across five well-distributed tropical sites. We find considerable regional and seasonal differences in trends. Specifically: (1) Only one SHADOZ site, in the equatorial Americas, exhibits a statistically significant annually averaged LMS ozone loss; the same station and one in the western Pacific display an annual positive FT ozone increase. (2) At the other sites, significant trends occur only in certain months: LMS ozone losses mid-year; FT ozone increases during periods of greatest convective activity (February-April, after July). (3) The LMS ozone losses are highly correlated with an increase in tropopause height but the latter only explains part of the LMS ozone loss. (4) The seasonal signal in SHADOZ FT ozone changes suggests a dynamical component in tropospheric ozone increases, extending across remote and urban regions. These SHADOZ-derived FT and LMS ozone trends, modest with respect to other recent satellite- or model-derived tropical trends, highlight regional and seasonal variability across the tropics and define a new reference for evaluating ozone changes over the 1998 to 2019 period.

**Plain Language Summary**

Understanding free troposphere (FT) and lowermost stratosphere (LMS) ozone variability is an important climate topic. LMS evaluations are based on satellite observations; FT ozone assessments rely on aircraft profiles. Ozonesonde measurements constitute an independent FT and LMS dataset. We used Southern Hemisphere Additional Ozonesondes data from 1998-2019 in a Multiple Linear Regression model to analyze FT and LMS ozone across five tropical sites. Our findings: (1) Only one station exhibits positive FT and negative LMS ozone trends. At the other sites, trends occur in isolated layers during months with changing convection. (2) Our LMS ozone trends are smaller than most satellite- and model-based analyses. (3) The LMS ozone trends over the course of the year correlate with changes in tropopause height (TH). (4) The ozone loss maximizes when TH increases maximize. These changes suggest a climate change signal but the TH trend only partially explains LMS ozone. (5) Large regions of the tropics do not display FT ozone increases. An absence of trends during the fire season over the south Atlantic and eastern Indian Ocean suggests that pyrogenic pollution there has not increased. Our regional and seasonal variations in ozone trends serve as a reference for satellite- and model-based analyses.

# 1 Introduction

## 1.1 Trends in Free Tropospheric and Lowermost Stratospheric Ozone

Trends in tropical free tropospheric (FT) ozone have been featured in studies that used model results (*Zhang et al.,* 2016), satellites (*Gaudel et al.,* 2018; *Ziemke et al.,* 2019) and commercial aircraft profiles (*Gaudel et al.,* 2020). *Gaudel et al.* (2018) summarize global uncertainties, displaying trends in tropical tropospheric ozone from five satellite-derived maps that disagree in magnitude and even sign. Changes based on various Aura/OMI (2005-2016) products ranged from ~(10-25)%/decade. In *Gaudel et al.* (2020) trends in FT ozone are +(3-5)%/decade) based on commercial aircraft data (http://iagos.org) from a small number of urban airports in the northern tropics.

Studies with satellite data, including Aura OMI and MLS, also reflect uncertainty in both LMS and FT ozone trends over the past 15-20 years. Recent work with merged satellite datasets (SWOOSH, GOZCARDS, Merged SBUV; *SPARC/IO3C/GAW*, 2019) in the mid to lower stratosphere, along with chemistry-transport models (*Stauffer et al.,* 2019) and ozone assimilations, indicate the uncertainty of possible LMS ozone trends (*Ball et al.,* 2018; *Chipperfield et al.,* 2018; *Wargan et al.,* 2018), at least on a zonally averaged basis. For example, the products summarized by *Ball et al.* (2018), suggest a 20-yr (1998-2016) lowermost stratospheric (LMS) ozone loss up to 5%/decade, whereas *Wargan et al.* (2018; Figure 3) show a comparable *increase* in LMS ozone over the same period. A new study (*Szelag et al.,* 2020) with four satellite products reports LMS ozone losses of (2-3)%/decade in the tropics, a value that agrees with the most recent analysis of satellite data and many models (*Ball et al.,* 2020).

Ozonesonde data are widely used by the scientific community for satellite validation and model evaluation, especially in the region from ~5-20 km, where uncertainties in most satellite measurements are relatively large and feedbacks among temperature, dynamics, ozone and water vapor are complex and important. SHADOZ (Southern Hemisphere Additional Ozonesondes; *Thompson et al.,* 2003a; 2012) is a 14-station tropical and subtropical network that has archived > 9000 profiles since 1998. We address uncertainties in tropical FT and LMS ozone trends with reprocessed v06 SHADOZ profiles (*Thompson et al.,* 2017; *Witte et al*., 2017; 2018) that are better resolved (100-150 m in the vertical) than satellite measurements below 20 km. There are several other advantages of SHADOZ data. The SHADOZ measurements are distributed across eight tropical stations (*Thompson et al.*, 2003a) and cover both troposphere and stratosphere, capturing geographical variability. The SHADOZ locations are relatively free of urban influence so trends in FT ozone represent changes in background ozone over a large segment of the tropics. Another advantage of the SHADOZ data is that potential temperature readings from the radiosondes that accompany the ozonesonde launches provide direct information on dynamical factors that might be related to oscillations and trends.

### 1.2 Variability in FT and LMS Ozone: Climate Oscillations and Convection

Early studies of FT and LMS ozone variability with SHADOZ profiles focused on convective influences (*Folkins et al.,* 2000; 2002) and biomass burning (*Oltmans et al.,* 2001) over the western Pacific. More generally, *Thompson et al.* (2003b) showed that a mixture of dynamical and chemical influences determines FT ozone seasonal patterns at all SHADOZ stations. This view has been confirmed in studies of field campaigns (*Swap et al.,* 2003; *Thouret et al.,* 2009) and satellite observations (*Nassar et al.,* 2009).

ENSO-perturbed patterns of convection, precipitation and fire lead to variability in FT and LMS ozone profiles that vary station to station (*Randel and Thompson,* 2011). In some cases, the ENSO leads to positive ozone anomalies; at other locations, ozone may decrease (*Thompson and Hudson,* 1999). *Thompson et al.* (2001) used sonde and satellite data to demonstrate that even when fires cause exceptional pollution, as over Indonesia in 1997-1998, dynamical anomalies like the ENSO and Indian Ocean Dipole are major factors in a tropospheric ozone buildup. Other studies linking dynamics and FT and LMS ozone variability have examined the QBO (*Witte et al.,* 2008). Compared to HALOE on UARS (Halogen Occultation Experiment, Upper Atmosphere Research Satellite), SHADOZ sonde profiles show more structure in the LMS. Employing different statistical approaches, *Lee et al.* (2010) and *Randel and Thompson* (2011) found that QBO and ENSO impacts on FT and LMS ozone varied among tropical stations (within ±12 degrees latitude) over the 11 years of SHADOZ (1998-2009).

*Thompson et al.* (2011) reported on convectively-generated wave activity in the LMS for ten stations over the first decade (1998-2007) of the SHADOZ record. Laminae in ozone and potential temperature profiles were used to identify vertical displacements in segments up to 20 km that are attributed to convectively-generated waves (*Grant et al*., 1998). Using a Gravity Wave Index (GWI) based on laminae frequency, ozone variations were linked to the ENSO cycle (*Thompson et al.,* 2011). Strong relationships between gravity waves and ozone vertical structure are also indicated when FT ozone profiles are classified by Self-Organizing Maps

(SOM; *Jensen et al.,* 2012; *Stauffer et al.,* 2018). The lowest ozone mixing ratios at SHADOZ stations coincide with the most intense connective activity, as indicated by wind velocity potential, geopotential height, cloud cover, etc. Profiles with the highest ozone mixing ratios occur under stable meteorological conditions along with elevated concentrations of pollutants as seen by satellite. Signatures of the Madden-Julian Oscillation in ozone variations over the western Pacific/eastern Indian Ocean have been reported in SHADOZ profiles (*Stauffer et al.,* 2018) and in satellite estimations of tropospheric ozone (*Ziemke and Chandra,* 2003).

### 1.3 This Study

The uncertainty in lower atmospheric ozone changes over the past two decades and the documented impact of seasonal convection and climate oscillations on tropical ozone are motivation for examining ozone variability and trends with the 22-year SHADOZ record. First, we review seasonal and regional variations in FT and LMS ozone SHADOZ observations and convective activity as signified by ozone and radiosonde laminae. Second, trends in ozone profiles from 1998-2019 are determined with a standard Multiple Linear Regression (MLR) model. To investigate possible mechanisms for FT and LMS ozone changes, the MLR model is also applied to tropopause height derived from the SHADOZ radiosondes. We address the following questions:

- What are the overall trends, if any, in LMS and FT ozone in the tropics?
- Are there regional and/or seasonal variations in the trends?
- Do the sonde data provide useful information on dynamical factors connected to trends?

Data and analysis methods appear in **Section 2** with Results and Discussion in **Section 3. Section 4** is a summary.

## 2. Data and Methods of Analysis

### 2.1 Reprocessed SHADOZ Data

Ozone data are taken from the SHADOZ archive (https://tropo.gsfc.nasa.gov/shadoz); the profiles measured originate from electrochemical concentration cell ozonesondes coupled to standard radiosondes. For analysis of tropical ozone, we use v06 data from eight of the 14 long-term stations (**Table 1**). For more reliable statistics three of the "stations" or "sites" as they are referred to (**Figure 1**), are based on combining profiles from pairs of launch locations abbreviated as follows: SC-Para for San Cristóbal-Paramaribo; Nat-Asc for Natal-Ascension; KL-

Java for Kuala Lumpur-Watukosek. The v06 data, reprocessed in 2016-2018, reduced inhomogeneities due to instrument or data-handling changes (*Witte et al.,* 2017; 2018) such that sonde total ozone column (TOC) amounts agree with ground-based or satellite data within 2% for all but one station. Data from a number of SHADOZ stations display a 3-6% dropoff in TOC after 2013 (*Sterling et al.,* 2018; *Stauffer et al.,* 2020) relative to satellite and/or ground-based readings. For the stations analyzed here, the dropoff is confined to readings above 50 hPa (~20 km) and does not affect the results.

### 2.2 FT and LMS Definitions

Illustrations in **Section 3** span the surface to 20 km and refer to two FT segments: 5-10 km; 10-15 km. We use 15-20 km for the LMS, because this is where convective impacts on waves maximize (*Thompson et al.,* 2011) and where *Randel et al.* (2007) identified a distinct ozone annual cycle driven by the Brewer-Dobson circulation. The LMS includes most of the tropical tropopause layer (13.5-18.5 km) and several km above the tropical cold-point and thermal lapse-rate tropopauses over the SHADOZ sites (*Selkirk et al.,* 2010; *Thompson et al.,* 2012).

### 2.3 Multiple Linear Regression Model (MLR)

In order to quantify factors leading to seasonal and interannual variability as well as trends, a standard MLR model (original version *Stolarski et al.,* 1991, updated in *Ziemke et al.,* 2019) is applied to monthly mean ozone profiles for the 5 stations: the 3 combined sites, Nairobi and Samoa. The model includes terms for annual and semi-annual cycles and oscillations prevalent in the tropics: QBO, MEI (Multivariate ENSO Index, v2) and IOD DMI (Indian Ocean Dipole Moment Index; only for KL-Java):

$$O_3(t) = A(t) + B(t)t + C(t)MEI(t) + D(t)QBO1(t) + E(t)QBO2(t) + F(t)IOD(t) + \varepsilon(t)$$

where t is month. The coefficients are as follows: A is periodic with 12, 6, 4, and 3 month cycles, and B through F have a period of 12 months, where A is the mean monthly seasonal cycle and B represents the month-dependent linear trend. The model includes data from the MEIv2 (https://www.esrl.noaa.gov/psd/enso/mei/), the two leading QBO EOFs from Singapore monthly mean zonal radiosonde winds at 10, 15, 20, 30, 40, 50, and 70 hPa levels, and IOD DMI (https://psl.noaa/gov/data/timeseries/DMI/). The $\varepsilon(t)$ is the residual, i.e., the difference between the best-fit model and the raw data. Monthly ozone data and model fits for the mid FT (5-10 km) and LMS (**Figures S1 and S2**) are well-correlated; for the LMS, for example, the correlation coefficients are r = 0.83-0.90 (**Figure S2**). The IOD DMI term is included only for KL-

Java, because that was the only station where the IOD DMI accounted for a statistically significant response in ozone in the MLR model.

The MLR model was separately applied to the monthly mean ozone profiles at 100 m resolution, and the monthly mean partial column ozone amounts from 5-10 km, 10-15 km, and 15-20 km. We also applied the MLR model to the monthly mean tropopause altitude at each station, defined as the 380 K potential temperature surface (e.g., *Wargan et al.*, 2018).

### 2.4 Laminar Identification (LID) and GW Indices

The Laminar Identification (LID) method was used to identify convective signatures in ozone profiles for the 1998-2009 SHADOZ data (*Thompson et al.,* 2011). The LID technique, applied here to the 1998-2019 record (**Table 1**), is based on the coherence of laminae in each ozone and potential temperature profile pair; laminae are identified as deviations from running means calculated every 0.5 km from surface to 20 km. When the potential temperature and ozone laminae at a given level are strongly correlated ($r > 0.7$), as often occurs in the LMS, the presence of a convectively-generated gravity wave (GW) is inferred. The GW occurrence is a proxy for a convective event. Convective influence is quantified by the monthly GW frequency (GWF), defined as the percent ratio of profiles exhibiting the GW signal relative to the total number of profiles within a given month.

### 2.5 Self-Organizing Maps (SOM)

We have used SOM, a machine-learning technique, to classify ozone profiles in terms of meteorological or chemical influences (*Stauffer et al.,* 2016). The entire set of ozone profiles for each station is ingested into the SOM code to obtain initial nodes (i.e., centroids or means for each cluster) via a linear interpolation between the two largest components of the ensemble. Subsequent iterations assign a given profile to its “best match” until a cluster mean is obtained. We adopt key elements of the procedure in *Stauffer et al.* (2018): 1) a four-cluster 2x2 SOM is used to avoid clusters with too few members for meaningful statistics (cf *Jensen et al.,* 2012); 2) SOM clusters are numbered 1 to 4 based on the cluster “mean” ozone profile. The result is a consistent definition of Cluster 1 and Cluster 4 as “low” and “high” ozone for each site, respectively. Links among SOM ozone profile shape, GWF, and trends will be investigated.

## 3 Results and Discussion

### 3.1 Seasonal Cycles in Ozone and Convective Influence

**Figure 2** displays the 5-site monthly ozone climatology from the surface to 20 km. Regional differences in vertical structure are pronounced. Red to yellow (~90-60 ppbv) colors never appear in mid FT ozone over the equatorial Americas (SC-Para, **Figure 2a**), KL-Java or Samoa (**Figures 2d,e**). Conversely, FT ozone values ≤ 30 ppbv never appear over Nat-Asc or Nairobi (**Figures 2b,c**). These contrasts partly reflect regional differences in ascending vs. descending nodes of the Walker circulation. The mean TOC over the south tropical Atlantic Ocean is 5% greater than over the western Pacific, giving rise to the well-known tropospheric zonal wave-one (*Thompson et al.,* 2003b). Compared to the FT, there is less regional variability in LMS ozone (Figure 8 in *Thompson et al.*, 2017). A large seasonal signal in LMS ozone is associated with the Brewer-Dobson circulation (**Figure 3a**; cf *Randel et al.,* 2007).

FT ozone seasonality is less uniform due to the timing of various dynamical and chemical influences across sites. However, the minima for all sites occur in January through April or May (**Figures 3b,c**) except for a second short minimum after July over Nairobi and KL-Java. Localized FT ozone maxima occur largely from imported fire pollution: SC-Para in March and after August; at KL-Java in April-May (**Figures 2a,d**); features at 6-8 km over Nat-Asc and Samoa August to November (**Figures 2b,e**); Nairobi (**Figure 2c**) in June and after August. Although month-to-month anomalies from annual mean FT ozone (**Figure 3b,c)** in the 5-10 km and 10-15 km layers, appear complex, there are 2-4 distinct transitions (**Figure 4**). The vertical dashed lines appearing on **Figures 2, 4, and 5** mark when ozone anomalies from the annual mean over 5-15 km change sign, indicating transitions in seasonal ozone amount and convective activity. Convective influence, given by GWF (**Figure 5**), with transitions marked as for ozone, shifts during the same periods. GWF reaches 50-70% February-April at all locations (**Figure 5**), during which ozone minima above 8 km, attributed to convective redistribution of near-surface lower ozone air (**Figure 2**), appear over all stations. Comparing **Figures 4 and 5** reveals the correspondence between increased (decreased) convective activity and decreased (increased) ozone amounts, especially in the upper FT and LMS.

### 3.2 FT and LMS Ozone Changes (1998-2019)

In **Figure 6** FT and LMS changes in ozone mixing ratio (%/decade during 1998-2019) are displayed, based on monthly mean trends computed with the MLR model. Corresponding values in three layers appear in **Table 1.** Shades of red (blue) in **Figure 6** represent ozone increases (decreases); cyan hatching denotes statistical (95%) significance. The annual mean trends in

**Table 1** are computed by taking the average of the 12 monthly trends in DU, and dividing by the mean seasonal ozone in DU to yield the annual percentage trend. The annual trend significance is assessed at the 95% confidence level as with the monthly trends.

#### 3.2.1 FT Ozone Trends

For all five stations in **Figure 6**, albeit very weakly at Nat-Asc, there is a pattern of significant ozone increase at various altitudes in the FT beginning in February. The largest trends are seen over SC-Para and KL-Java (**Figures 6a,d**). The increases in column-integrated ozone for those stations in the 5-10 km and 10-15 km layers (bold and underlined values indicate statistical significance in **Table 1**), correspond to an annual trend of +(2-4)%/decade and ~6%/decade in the 5-10 km and 10-15 km layers, respectively (**Table 1**).

The dominant impact of southern African and South American fires on Nat-Asc and Samoa FT ozone in July through November is well-documented (*Oltmans et al*., 2001; *Thompson et al.,* 2003b). A near-absence of trends over these sites in the second half of the year (**Figures 6b,e)** signifies little change in fires since 1998, consistent with a lack of trends in pyrogenic $NO_x$ over the past 25 years reported in *Gaudel et al.* (2020; Figure 5). There is also a notable absence of a positive FT ozone over KL-Java in the August to October period, which is the typical fire season in Indonesia (*Pan et al.,* 2018). FT ozone increases over KL-Java (**Figure 6d**) in February-March may be related to the southeast Asian fire season (*Ogino et al.,* 2020) and/or to growing urban emissions (*Zhang et al.,* 2016; *Gaudel et al.*, 2020).

The annual cycles of FT ozone (**Figures 3b,c**) provide context for the changes shown in **Figure 6** and **Table 1.** The column-integrated ozone changes (5-10 km and 10-15 km) are never significantly negative for any month except for October at Nairobi. In the mid FT (5-10 km), ozone trends are significantly positive only in the lowest-ozone, convectively active time of year (February to May; **Figure 6**).

*Zhang et al.* (2016) and *Gaudel et al.* (2018) presented analyses of tropospheric ozone changes at different periods within 1994-2015. In those studies, both satellite-derived tropospheric ozone columns and commercial aircraft profiles include ozone below 5 km. Thus, it is not surprising that that the *Zhang et al.* (2016) and *Gaudel et al.* (2018) trends exceed the FT changes calculated here. A direct comparison of the FT segments of KL-Java SHADOZ sondes with Malaysia-labeled aircraft (IAGOS) profiles in *Gaudel et al.* (2020) displays a different sampling distribution. The mixing ratios are 50% greater than in the SHADOZ profiles, likely because the *Gaudel et al.* (2020) "Malaysia" data include landing/takeoffs at Jakarta, Indonesia. The FT ozone changes for "Malaysia" in *Gaudel et al.* (2020) over the period 1995 to 2016 are ~+5%/decade, similar to our KL-Java FT trends of +(2-5)%/decade (**Table 1**).

The satellite trends, for example, in *Zhang et al.* (2016; supplement Figure 21, covering 2004-2015) are relatively small and in reasonable agreement with the SHADOZ-derived FT ozone changes for SC-Para and KL-Java (**Figures 6a,d**). However, they do not agree with SHADOZ trends over the Atlantic, Nairobi and Samoa; the satellite picture implies the trends are more widespread than the sonde data. Preliminary comparisons of our SHADOZ results with trends from a typical OMI-derived column product (*Ziemke et al.,* 2019) show that the monthly changes in satellite columns are never negative whereas **Figures 6c** and **6d** show some FT layers with significant ozone loss. It is important to note that satellite tropospheric columns probably include some lower-tropospheric pollution that our study excludes. Note, that of the three OMI-based satellite trends reviewed by *Gaudel et al.* (2018; Figure 24), the OMI/MLS displays the smallest changes.

### 3.2.2 LMS Ozone Trends

**Figures 6c** and **6d** show signatures of early-year (February-April/May) increases in LMS ozone over Nairobi and KL-Java. Note that the structure of the changes over Nairobi and KL-Java suggests decoupling of the LMS and FT ozone trends (**Figure 6c,d**). At SC-Para (**Figure 6a**) LMS ozone losses set in after May, extending in some layers to December. Mid- to late-year LMS ozone losses are found at all other sites; for Samoa (**Figures 6e**) there is only a thin layer with statistically significant ozone loss in December and January. **Table 1** (bold, underlined values) shows that these LMS losses are significant only in isolated months. Consequently, there is no annually averaged trend except at SC-Para with (-3.0)%/decade loss in LMS ozone (**Table 1**; similar to the statistically insignificant trends found at KL-Java and Samoa). This is consistent with the magnitude of updated satellite-based and model trends reported recently by *Ball et al.* (2020) who display only zonal averages with no reference to regional trends. If the SHADOZ-based losses are confined to only one area, the zonally averaged negative trends may be overestimating LMS ozone losses in the tropics.

The first study of seasonality in lower stratospheric ozone trends – results reported as zonal means for four merged satellite products – was published by *Szelag et al.* (2020). For all four products, the season with the most negative trend is March-April-May, not June through

September as for the SHADOZ stations in **Figure 6** and **Table 1.** However, the *Szelag et al.* (2020; Figure 4) calculations are not shown below 19 km, so they are not directly comparable to our analyses.

In contrast to the highly varied seasonal patterns of FT ozone (**Figures 3b,c**), the annual cycle of LMS ozone (**Figure 3a**) is fairly uniform (*Randel et al.,* 2007). A comparison with the LMS trends in **Figure 6** shows that (1) largely insignificant ozone increases occur only during the low-ozone time of year (January to May) with (2) more sustained negative LMS ozone trends taking place during the maximum-ozone period (June/July through October/November; **Figure 3a**). This means that over the year the magnitude of the annual LMS seasonal cycle has declined slightly, i.e., the annual cycle is flattening.

### 3.3 Dynamic Influences in Ozone Trends

#### 3.3.1 Trends in Tropopause Height

**Figure 7** illustrates the trends in monthly LMS ozone (**Figure 7a**, %/decade) and TH (**Figure 7b**, trend in the altitude of 380 K potential temperature [θ] surface in m/decade) as computed from the MLR model for three stations. After June, when the ozone loss is most pronounced over SC-Para, Nat-Asc and Nairobi, there is an increase in TH (**Figure 7b**) that is correlated with the LMS ozone decrease (r = 0.7 to 0.91). This relationship is strong at Samoa as well (not shown) although the largest ozone loss and TH increase occur there in April and May. Because the LMS definition here is 15-20 km, it is reasonable to ask if increased tropopause height (a stratospheric (tropospheric) thickness reduced (increased) by 100-200 m) is partially responsible for the LMS ozone loss. To examine this, we applied the monthly TH height trends to the MLR ozone seasonal cycle (MLR term A(t)) by shifting the ozone profiles at SC-Para, Nat-Asc, and Nairobi by the TH trend amount each month. The 15-20 km seasonal ozone changes implied from the TH trends correlate well (r = 0.67-0.9) with the MLR-calculated ozone trends from 15-20 km (**Figure 8**). However, the TH trends only partially explain the LMS ozone trends. They coincide closely in July (all stations shown) and in August and September for SC-Para and Nat-Asc (**Figures 8a,b**). However, the TH-induced change does not account for the ozone trend over Nat-Asc from January to May (**Figure 8b**) and falls short over Nairobi from September through January (**Figure 8c**).

#### 3.3.2 Role of Convection

**Sections 3.1 and 3.2** described an implicit role for convection in the seasonal variability of FT and LMS ozone. Here, we examine links between ozone profile variability and convection using the LID and SOM methods (**Sections 2.4** and **2.5**). The classification of ozone profiles for several SHADOZ sites in a 2x2 SOM (*Stauffer et al.,* 2018) established an anticorrelation between FT ozone mixing ratios and convective activity, where the latter was quantified by meteorological parameters at sonde launch time (Figure 7 in *Stauffer et al.,* 2018). The SOM in **Figure 9** shows similar relationships. Clusters displaying the lowest (Cluster 1) and highest (Cluster 4) profiles of ozone are illustrated. The characteristic S-shapes of upper FT ozone profiles in Cluster 1 (**Figure 9a)** display the lowest mixing ratios whereas much of the elevated ozone in Cluster 4 (**Figure 9b)** derives from imported pollution at 5-10 km. The GWF corresponding to Cluster 1 (**Figure 9c)**, representing maximum convection, is dominated by January-May profiles (**Figure 9e**), that is, when there are positive FT ozone changes at all sites except Samoa. Cluster 4 ozone mixing ratios throughout the FT and LMS (**Figure 9b**) are much greater than Cluster 1 (**Figure 9a**) throughout the FT and LMS and correspond to the season when the stations are most affected by transported pollution from biomass fires (**Figure 9f**). The fire season impacts are strongest from June through November except for KL-Java where a March through May maximum corresponds to the heaviest burning in southeast Asian fire (the seasonality can be modified under conditions of a major ENSO; *Thompson et al.,* 2001; *Field et al.,* 2016; *Pan et al.,* 2018). **Figure 9d** shows that for all stations, convection as indicated by GWF is greatly reduced during the burning season. GWF in Cluster 4 (**Figure 9d**) remains near 50% for KL-Java with April and October the most prevalent months; the latter coincides with the later Asian monsoon period.

The connection of the ozone trends to convection using the GWF proxy is not clear, but there are correlations among GWF changes and ozone trends. For example, computing the difference in GWF for the first five years (1998-2002) and the latest five years (2015-2019) in the SHADOZ record (**Figure 10**) shows correspondence among increasing GWF and decreasing LMS ozone, and decreasing GWF and increasing FT ozone. At all sites the GWF declines during the first 2-4 months of the year when segments of FT ozone are increasing (**Figure 6**)**.** If there is less convection, signifying less vertical mixing and detrainment, FT ozone would accumulate. Mid-year, particularly over SC-Para, KL-Java, and Samoa (**Figures 10a,d,e**), GWF increases greatly. Inasmuch as ozone is decreasing during this time (**Figures 6** and **7**), this means that increased convection may play a role in observed ozone trends in the LMS near the tropopause. The interaction among changes in convection, which are highly uncertain, and trends in ozone and TH cannot be determined from the SHADOZ sonde data alone. Independent data, e.g., OLR, dynamical parameters from re-analyses and model simulations need to be examined.

## 4 Summary

The 22-year SHADOZ record (1998-2019) of ozone profiles from five well-distributed tropical regions has been used to compute trends in the FT (5-15 km) and LMS (15-20 km). Only at one station, SC-Para, is there an annually averaged FT ozone increase, ~5%/ decade along with an annual LMS ozone loss, -3.0%/decade. At KL-Java, FT ozone (10-15 km) has an annual increase of +5%/dec. Changes in FT ozone vary considerably from site to site, with four of five stations displaying significant increases during February to April when the TH has a small negative trend. The FT ozone trends may be related to reduced convective activity indicated by changes to GWF.

LMS ozone losses later in the year take place when GWF convective influence and TH tropopause altitude are both increasing. The LMS ozone and TH trends are strongest between June and August/September. We showed that the decrease in LMS ozone may be caused by the TH increase during this period but the TH changes do not explain LMS ozone trends at other times of the year. Because the LMS ozone decline maximizes at the annual ozone maximum without a comparable increase at other times of year, the annual ozone cycle associated with the Brewer-Dobson Circulation is flattening over time. The TH increase occurs during the annual TH minimum and the magnitude of the tropopause cycle is also diminished.

*Randel et al.* (2007) and *Stolarski et al.* (2014) used satellite observations and meteorological analyses to describe multiple dynamical influences on LMS ozone. Our simplified study interprets FT and LMS ozone changes with reference to TH and a proxy for vertical motion that is inferred only from the sounding data. Model diagnostics are required to assess the roles of changing chemistry in the troposphere and to evaluate the contributions of perturbed dynamics to FT and LMS ozone changes. Nonetheless, the relatively small, geographically distinct changes derived from SHADOZ profiles provide a reference for evaluating (1) LMS ozone trends derived from satellite products that do not include regional variability (*Ball et al.,* 2020; *Szelag et al.,* 2020) and (2) aircraft-based (*Gaudel et al.,* 2020) FT ozone trends that are biased toward urban areas. The SHADOZ trends suggest that large regions of the tropics do not show year-round FT ozone increases. It is possible that increases in tropical tropospheric ozone have dynamical origins and are not a consequence of growing anthropogenic emissions alone. This first report of an increasing tropopause height over SHADOZ sites is also a reference for satellite observations and models.

**Acknowledgments**

Support is gratefully acknowledged from the NASA Upper Air Research Program (K. W. Jucks, Program Manager), S-NPP and JPSS (J. F. Gleason, Project Scientist) and the NASA Post-doctoral Program to RMS. We are grateful to O. R. Cooper (CIRES/NOAA-CSL) and W. Randel (NCAR) for helpful comments. SHADOZ v06 profile data are available at https://tropo.gsfc.nasa.gov/shadoz/Archive.html.

## References

Ball, W. T., Alsing, J., Mortlock, D. J., Staehelin, J., Haigh, J. D., Peter, T., et al. (2018). Continuous decline in lower stratospheric ozone off sets ozone layer recovery, *Atmos. Chem. Phys.*, 18, 1379–1394, https://doi.org/10.5194/acp-18-1379-2018

Ball, W. T., Chiodo, G., Abalos, M., Alsing, J., Stenke, A. (2020) Inconsistencies between chemistry-climate models and observed lower stratospheric ozone trends since 1998, *Atmos. Chem. Phys.*, 20, 9737–9752. https://doi.org/10.5194/acp-20-9737-2020

Chipperfield, M. P., Dhomse, S., Hossaini, R., Feng, W., Santee, M. L., Weber, M., et al. (2018). On the cause of recent variations in lower stratospheric ozone, *Geophys. Res. Lett.*, 45, https://doi.org/10.1029/2018GL078071

Field, R. D., van der Werf, G. R., Fanin, T., Fetzer, E. J., Fuller, R., Jethva, H., et al. (2016) Indonesian fire activity and smoke pollution in 2015 show persistent nonlinear sensitivity to El Niño-induced drought, *Proc. Natl. Acad. Sci. USA.* 2016 Aug 16; 113(33): 9204–9209. 10.1073/pnas.1524888113

Folkins, I., Oltmans, S. J., Thompson, A. M., (2000) Tropical convective outflow and near-surface equivalent potential temperatures, *Geophys. Res. Lett.,* 27, 2549-2552

Folkins, I. Braun, C., Thompson, A. M., Witte, J. C. (2002). Tropical ozone as in indicator of deep convective outflow, *J. Geophys. Res.*, 107, D13, doi: 10.1029/2001JD001178

Gaudel, A., Cooper, O. R., Ancellet, G., Barret, B., Boynard, A., Burrows, J. P., et al. (2018). Tropospheric Ozone Assessment Report: Present-day distribution and trends of tropospheric ozone relevant to climate and global atmospheric chemistry model evaluation, *Elem. Sci. Anth.*, 6: 39, doi: https://doi.org/10.1525/elementa.291

Gaudel, A., Cooper, O. R, Chang, K.-L., Bourgeois, I., Ziemke, J. R., Strode, S. A., Oman, L. D., et al. (2020). Aircraft observations since the 1990s reveal increases of tropospheric ozone at multiple locations across the Northern Hemisphere*, Science Advances,* 6, no. 34, eaba8272, doi: 10.1126/sciadv.aba8272

Grant, W. B., Pierce, R. B., Oltmans, S. J., Browell, E. V. (1998), Seasonal evolution of total and gravity wave induced laminae in ozonesonde data in the tropics and subtropics, *Geophys. Res. Lett.,* 25, 1863‐1866, doi:10.1029/98GL01297

Jensen, A. A., Thompson, A. M., Schmidlin, F. J. (2012). Classification of Ascension Island and Natal ozonesondes using self-organizing maps, *J. Geophys. Res*., 117, D04302, doi10.1029/2011JD016573

Lee, S., Shelow, D. M., Thompson, A. M., Miller, S. K. (2010). QBO and ENSO variability in temperature and ozone from SHADOZ (1998-2005), *J. Geophys. Res.,* 115, D18105, doi: 10.1029/2009JD013320

Nassar, R., Logan, J. A., Megretskaia, I. A., Murray, L. T., Zhang, L., Jones, D. B. A. (2009) Analysis of tropical tropospheric ozone, carbon monoxide, and water vapor during the 2006 El Niño using TES observations and the GEOS-Chem model, *J. Geophys. Res.,* https://doi.org/10.1029/2009JD011760

Ogino, S.-Y., Fujiwara, M. Shiotani, M., Hasebe, F., Matsumoto, T., Hoang, T. H. T., Nguyen, T. T. T. (2013) Ozone variations over the northern subtropical region revealed by ozonesonde observations in Hanoi*, J. Geophys. Res. Atmos*. 118, 3245–3257, doi:10.1002/jgrd.50348

Oltmans, S. J., Johnson, B. J., Harris, J. M., Vömel, H., Thompson, A. M., et al. (2001). Ozone in the Pacific tropical troposphere from ozonesonde observations*, J. Geophys. Res.,* 106, 32503-32526, doi: https://doi.org/10.1029/2000JD900834

Pan, X., Chin, M., Ichoku, C. M., Field, R. D. (2018) Connecting Indonesian Fires and Drought With the Type of El Niño and Phase of the Indian Ocean Dipole During 1979–2016, *J. Geophys. Res.,* https://doi.org/10.1029/2018JD028402

Randel, W. J., Park, M., Wu, F. (2007). A large annual cycle in ozone above the tropical tropopause linked to the Brewer–Dobson circulation, *J. Atmos. Sci.*, 64, 4479-4488, doi: 10.1175/2007JAS2409.1

Randel, W. J., and Thompson, A. M. (2011), Interannual variability and trends in tropical ozone derived from SHADOZ ozonesondes and SAGE II satellite data, *J. Geophys. Res*., 116, D07303, doi:10.1029/ 2010JD015195

Selkirk, H. B., Vömel, H., Valverde Canossa, J. M., Pfister, L., Diaz, J. A., Fernández, W., et al. (2010) Detailed structure of the tropical upper troposphere and lower stratosphere as revealed by balloonsonde observations of water vapor, ozone, temperature and winds during the NASA TCSP and TC$^4$ Campaigns, *J. Geophys. Res*., 115, https://doi.org/10.1029/2009JD013209

SPARC/IO3C/GAW (2019). SPARC/IO3C/GAW Report on Long-term Ozone Trends and Uncertainties in the Stratosphere, I. Petropavlovskikh, S. Godin-Beekmann, D. Hubert, R. Damadeo, B. Hassler, V. Sofieva (Eds.), SPARC Report No. 9, GAW Report No. 241, WCRP-17/2018, doi: 10.17874/f899e57a20b; www.sparc-climate.org/publications/sparc-reports

Stauffer, R. M., Thompson, A. M., Witte, J. C. (2018). Characterizing global ozonesonde profile variability from surface to the UT/LS with a clustering technique and MERRA-2 reanalysis, *J. Geophys. Res. Atmos*., 123, 6213–6229, https://doi.org/10.1029/2018JD028465

Stauffer, R. M., Thompson, A. M., Kollonige, D. E., Witte, J. C., Tarasick, D. W., Davies, J., et al. (2020). A post-2013 dropoff in total ozone at a third of global ozonesonde stations: Electrochemical concentration cell instrument artifacts? *Geophys. Res. Lett*., 47, e2019GL086791. https://doi.org/10.1029/2019GL086791

Sterling, C. W., Johnson, B. J., Oltmans, S. J., Smit, H. G. J., Jordan, A. F., Cullis, P. D., et al. (2018). Homogenizing and estimating the uncertainty in NOAA's long-term vertical ozone profile records measured with the electrochemical concentration cell ozonesonde, *Atmos. Meas. Tech*., 11, 3661-3687, https://doi.org/10.5194/amt-11-3661-2018

Stolarski, R. S., Bloomfield, P. R., McPeters, R. D., Herman, J. R. (1991). Total ozone trends deduced from Nimbus 7 TOMS data, *Geophys. Res. Lett*., 18, 1015-1018, https://doi.org/10.1029/91GL01302

Stolarski, R. S., Waugh, D. W., Wang, L., Oman, L. D., Douglass, A. R., Newman, P. A. (2014). Seasonal variation of ozone in the tropical lower stratosphere: Southern tropics are different from northern tropics, *J. Geophys. Res. Atmos*., 119, 6196–6206, doi:10.1002/2013JD021294

Swap, R. J., Annegarn, H. J., Suttles, J. T., Haywood, J., Hemlinger, M. C., et al., (2002). The Southern African Regional Science Initiative (SAFARI-2000): Dry-Season Campaign, an Overview, *S. Afr. J. Science*, 98, 125-130

Szeląg, M. E., Sofieva, V. F., Degenstein, D., Roth, C., Davis, S., and Froidevaux, L. (2020). Seasonal stratospheric ozone trends over 2000–2018 derived from several merged data sets, *Atmos. Chem. Phys*., 20, 7035–7047, https://doi.org/10.5194/acp-20-7035-2020

Thompson, A. M., and Hudson, R. D. (1999) Tropical Tropospheric Ozone (TTO) maps from Nimbus-7 and Earth-Probe TOMS by the modified-residual method: Evaluation with sondes, ENSO signals and trends from Atlantic regional time series, *J. Geophys. Res.,* 26,961-26,975

Thompson, A. M., Witte, J. C., Hudson, R. D., Guo, H., Herman, J. R., Fujiwara, M. (2001) Tropical tropospheric ozone and biomass burning, *Science,* 291, 2128-2132

Thompson, A. M., Witte, J. C., McPeters, R. D., Oltmans, S. J., Schmidlin, F. J., J. A. Logan, J. A., et al. (2003a) Southern Hemisphere ADditional Ozonesondes (SHADOZ) 1998-2000 tropical ozone climatology. 1. Comparison with TOMS and ground-based measurements, J. Geophys. Res., 108, 8238, doi: 10.1029/2001JD000967

Thompson, A. M., Witte, J. C., Oltmans, S. J., Schmidlin, F. J., Logan, J. A., et al. (2003b) Southern Hemisphere ADditional Ozonesondes (SHADOZ) 1998-2000 tropical ozone climatology. 2. Tropospheric Variability and the zonal wave-one, *J. Geophys. Res. Atmos.,* 108, 8241, doi: https://doi.org/10.1029/2002JD002241

Thompson, A. M., Allen, A. L., Lee, S. Miller, S. K., Witte, J. C. (2011). Gravity and Rossby wave signatures in the tropical troposphere and lower stratosphere based on Southern Hemisphere Additional Ozonesondes (SHADOZ), 1998–2007, *J. Geophys. Res*., 116, D05302, doi:10.1029/2009JD013429

Thompson, A. M., Miller, S. K., Tilmes, S., Kollonige, D. W., Witte, J. C., et al. (2012). Southern Hemisphere Additional Ozonesondes (SHADOZ) tropical ozone climatology: Tropospheric and tropical tropopause layer (TTL) profiles with comparisons to OMI based ozone products. *J. Geophys. Res*., 117, D23301, doi: 10.1029/2010JD016911

Thompson, A. M., Witte, J. C., Sterling, C., Jordan, A., Johnson, B. J., Oltmans, S. J., et al. (2017). First reprocessing of Southern Hemisphere Additional Ozonesondes (SHADOZ) ozone profiles (1998–2016): 2. Comparisons with satellites and ground-based instruments, *J. Geophys. Res. Atmos*., 122, 13,000–13,025, https://doi.org/10.1002/2017JD027406

Thouret, V., Saunois, M., Minga, A., Mariscal, A., Sauvage, B., Solete, A., et al. (2009) An overview of two years of ozone radio soundings over Cotonou as part of AMMA, *Atmos. Chem. Phys.,* 9, 6157–6174, https://doi.org/10.5194/acp-9-6157-2009

Wargan, K., Orbe, C., Pawson, S., Ziemke, J. R., Oman, L. D., Olsen, M. A., et al. (2018). Recent decline in extratropical lower stratospheric ozone attributed to circulation changes, *Geophys. Res. Lett*., 45, 5166–5176, https://doi.org/10.1029/2018GL077406

Witte, J. C., Thompson, A. M., Smit, H. G. J., Fujiwara, M., Posny, F., et al. (2017). First reprocessing of Southern Hemisphere ADditional Ozonesondes (SHADOZ) profile records (1998-2015): 1. Methodology and evaluation, *J. Geophys. Res. Atmos*., 122, doi:10.1002/2016JD026403

Witte, J. C., Thompson, A. M., Smit, H. G. J., Fujiwara, M., Johnson, B. J., et al. (2018). First reprocessing of Southern Hemisphere ADditional Ozonesondes (SHADOZ) profile records (1998-2016): 3. Methodology and evaluation, *J. Geophys. Res. Atmos*., 123, doi:10.1002/2017JD027791

Zhang, Y. Cooper, O. R., Gaudel, A., Thompson, A. M., Nédelec, P., Ogino, S.-Y., West, J. J. (2016). Equatorward redistribution of emissions dominates the 1980 to 2010 tropospheric ozone change, *Nature-Geoscience*, doi: 10.1038/NGEO282

Ziemke, J. R., and Chandra, S. (2003) A Madden-Julian Oscillation in tropospheric ozone, *Geophys. Res., Lett.,* https://doi.org/10.1029/2003GL018523

Ziemke, J. R., Oman, L. D., Strode, S. A., Douglass, A. R., Olsen, M. A., et al. (2019). Trends in Global Tropospheric Ozone Inferred from a Composite Record of TOMS/OMI/MLS/OMPS Satellite Measurements and the MERRA-2 GMI Simulation, *Atmos. Chem. Phys*. 19, 3257–3269, doi: https://doi.org/10.5194/acp-19-3257-2019

## Figure Captions

Table 1. SHADOZ site metadata including number of profiles and index terms used in MLR ozone calculations. Monthly MLR partial column ozone linear trends are shown in percent per decade, with significant trends in bold and underlined. Significant annual trends occur only at SC-Para (all levels) and KL-Java (10-15 km).

Figure 1. Map of SHADOZ stations used in this study. Stations whose combined records are examined are colored orange (San Cristóbal and Paramaribo), red (Natal and Ascension), and blue (Kuala Lumpur and Watukosek). Samoa and Nairobi records are studied individually and colored gray. Sample numbers appear in **Table 1.**

Figure 2. Monthly averaged ozone mixing ratios from the surface to 20 km altitude for the five sites: two individual and three combinations. Both white and black contours are shown for the ozone mixing ratios for clarity. White dashed lines indicate transition periods marked by changes in sign of ozone anomalies from annual mean (see Section 3.1).

Figure 3. Seasonal ozone variability, expressed as percent anomaly from annual mean, from the MLR model in the LMS (a), FT (b and c). Tropopause Height (TH) is (d) based on the 380 K potential temperature surface from the radiosondes.

Figure 4. Monthly averaged $O_3$ mixing ratio anomalies in percent from the annual mean from the surface to 20 km altitude for the two individual and three combination sites. Black dashed lines (same as the white dashed lines in **Figure 2**) indicate transition periods marked by sign changes to the climatological FT and LMS $O_3$ amounts (see Section 3.1).

Figure 5. Monthly averaged gravity wave frequency (GWF) in percent from 10 to 20 km altitude corresponding to the profiles in Figure 2 for the two individual and three combination sites. White dashed lines are set by the ozone seasonal transitions as shown as in **Figures 2 and 4.**

Figure 6. Monthly MLR ozone linear trends from 5 to 20 km in percent per decade for the two individual and three combination sites. Positive trends are shown in red and negative trends are shown in blue. Trends that are significant with 95% confidence are shown with cyan hatching.

Figure 7. Monthly MLR trends in (a) LMS ozone column changes derived from SHADOZ sondes at the three indicated sites; (b) corresponding TH trends from the radiosondes. Dots represent the values and the error bars indicate the 95% confidence intervals.

Figure 8. Monthly MLR LMS ozone trends and error bars in percent per decade (black), and LMS ozone change induced by shifting the MLR seasonal ozone profiles by the TH trend in m per decade (red). (a) SC-Para, (b) Nat-Asc, (c) Nairobi.

Figure 9. (a, b): SOM cluster ozone means for the two individual and three combination sites. The number and percentage of profiles contributing to each of four clusters (two not shown) appear in each frame. (c, d): Gravity wave frequency (GWF in text) as a function of altitude corresponding to SOM clusters 1 and 4. Average percentage GWF from 15 to 20 km (LMS) for each site is shown in the frames. (e, f) monthly frequency distribution for the profiles corresponding to the SOM clusters.

Figure 10. Change in monthly GWF over two periods (2015-2019 minus 1998-2002) from 10 to 20 km altitude. Increases in GWF are shown in red, and decreases in GWF are shown in blue for the two individual and three combination sites.

Figure S1. Monthly averaged MLR (grey lines) and ozonesonde (black dots) ozone mixing ratios for the two individual and three combination sites in the 5 to 10 km layer. Correlations between MLR model fits and ozonesonde data are shown in each legend.

Figure S2. Monthly averaged MLR (grey lines) and ozonesonde (black dots) ozone mixing ratios for the two individual and three combination sites in the 15 to 20 km (LMS) layer. Correlations between MLR model fits and ozonesonde data are shown in each legend.

Trends by Layer in Percent Per Decade

| Site | Lat, Lon (°) | Profiles | MLR Terms | Jan | Feb | Mar | Apr | May | Jun | Jul | Aug | Sep | Oct | Nov | Dec | Ann |
|---|---|---|---|---|---|---|---|---|---|---|---|---|---|---|---|---|
| SC+Para | 5.8, -55.21/-0.92, -89.62 | 1227 | ENSO+QBO | | | | | | | | | | | | | |
| 5-10 km | | | | -3.1 | 6.1 | **12.7** | **9.5** | 3.8 | 4.7 | 6.6 | 4.2 | 2.3 | 3.9 | 3.3 | -2.3 | **4.2** |
| 10-15 km | | | | -1.6 | 0.0 | 9.3 | **13.2** | 3.5 | -0.9 | 4.0 | **9.4** | **9.7** | **10.4** | **10.9** | 5.5 | **6.2** |
| 15-20 km | | | | -2.2 | 0.7 | 1.4 | 0.0 | -0.9 | -2.1 | -4.7 | **-7.0** | **-6.4** | -3.8 | -2.6 | -3.3 | -3.0 |
| Natal+Ascen | -5.42, -35.38/-7.58, 14.24 | 1436 | ENSO+QBO | | | | | | | | | | | | | |
| 5-10 km | | | | 0.9 | -0.4 | -2.0 | -1.5 | 3.0 | 5.9 | 3.9 | 0.0 | -2.4 | -2.4 | -1.0 | 0.5 | 0.1 |
| 10-15 km | | | | 5.5 | 6.6 | 3.0 | -1.3 | -0.3 | 4.3 | 6.6 | 5.0 | 2.0 | 0.5 | 0.5 | 2.3 | 2.9 |
| 15-20 km | | | | 3.4 | 5.6 | 3.9 | 4.8 | 7.3 | 2.8 | -3.6 | **-5.4** | -3.0 | -1.4 | -2.2 | -0.9 | 0.3 |
| Nairobi | -1.27, 36.8 | 941 | ENSO+QBO | | | | | | | | | | | | | |
| 5-10 km | | | | 2.5 | **10.1** | **14.0** | 6.4 | -3.3 | -4.8 | -1.1 | 0.7 | -0.8 | -1.1 | 0.2 | 0.3 | 1.4 |
| 10-15 km | | | | 0.3 | 4.6 | 8.9 | 7.6 | 2.4 | 0.4 | 1.2 | -2.5 | -7.3 | **-6.9** | -3.2 | -0.7 | -0.1 |
| 15-20 km | | | | 3.0 | 5.6 | 7.4 | 6.0 | 1.4 | -2.8 | -4.0 | -2.9 | -1.1 | 0.2 | 0.7 | 1.3 | 0.6 |
| KL+Java | 2.73, 101.27/-7.5, 112.6 | 786 | ENSO+QBO+IOD | | | | | | | | | | | | | |
| 5-10 km | | | | -1.5 | **15.6** | **22.5** | **8.8** | -1.2 | -1.2 | 1.6 | 0.5 | -0.3 | 0.1 | -3.2 | -7.6 | 2.2 |
| 10-15 km | | | | -0.8 | 9.2 | **25.8** | **26.9** | **12.4** | 1.8 | 0.2 | 4.5 | 3.3 | -1.6 | -3.8 | -4.1 | 5.3 |
| 15-20 km | | | | **-9.1** | -2.9 | 1.7 | 3.8 | 4.4 | 1.3 | -3.5 | -5.7 | -3.5 | -2.5 | -6.6 | **-10.4** | -3.0 |
| Samoa | -14.23, -170.56 | 795 | ENSO+QBO | | | | | | | | | | | | | |
| 5-10 km | | | | 7.0 | 6.3 | 6.4 | 2.4 | -1.4 | -0.6 | 0.5 | -2.6 | -5.4 | -2.6 | 3.8 | 7.7 | 1.4 |
| 10-15 km | | | | 5.1 | 13.9 | 17.1 | 12.4 | 1.9 | -2.5 | -1.6 | 1.4 | 1.7 | -1.3 | -3.5 | -1.9 | 2.4 |
| 15-20 km | | | | -4.0 | 0.8 | 0.4 | -6.0 | -7.5 | -2.6 | 0.0 | -2.1 | -3.5 | -2.6 | -2.9 | -5.1 | -2.9 |

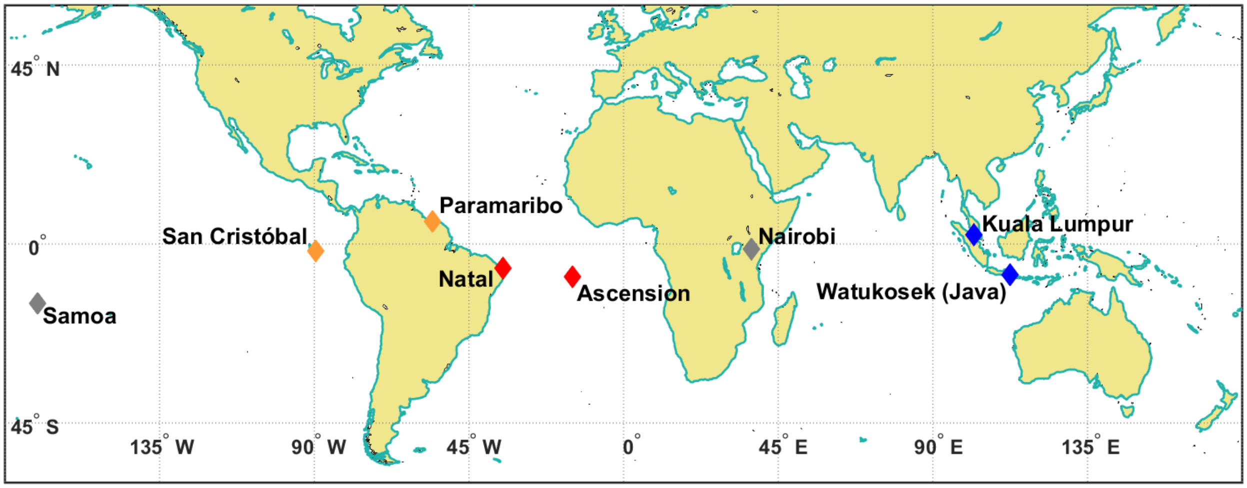


Figure 1. Map of SHADOZ stations used in this study. Stations whose combined records are examined are colored orange (San Cristóbal and Paramaribo), red (Natal and Ascension), and blue (Kuala Lumpur and Watukosek). Samoa and Nairobi records are studied individually and colored gray. Sample numbers appear in **Table 1.**

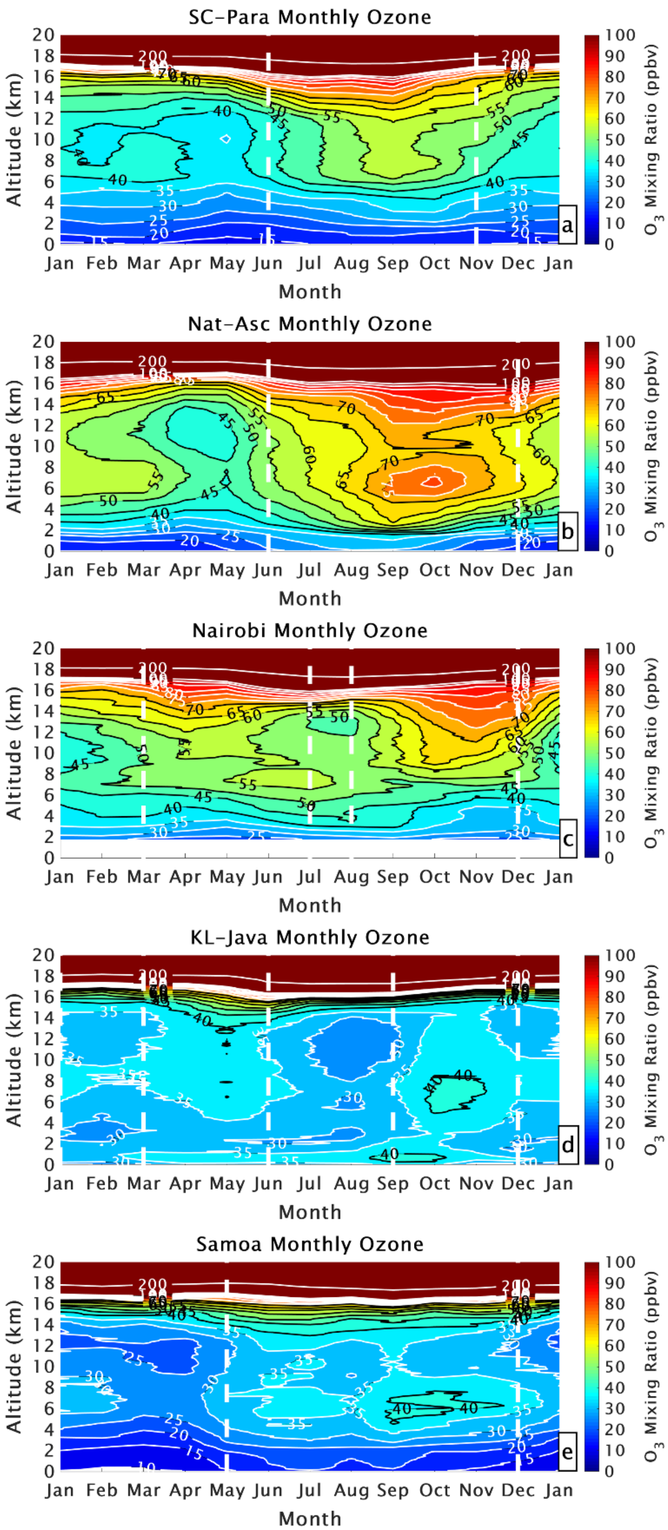


Figure 2. Monthly averaged ozone mixing ratios from the surface to 20 km altitude for the five sites: two individual and three combinations. Both white and black contours are shown for the ozone mixing ratios for clarity. White dashed lines indicate transition periods marked by changes in sign of ozone anomalies from annual mean (see Section 3.1).

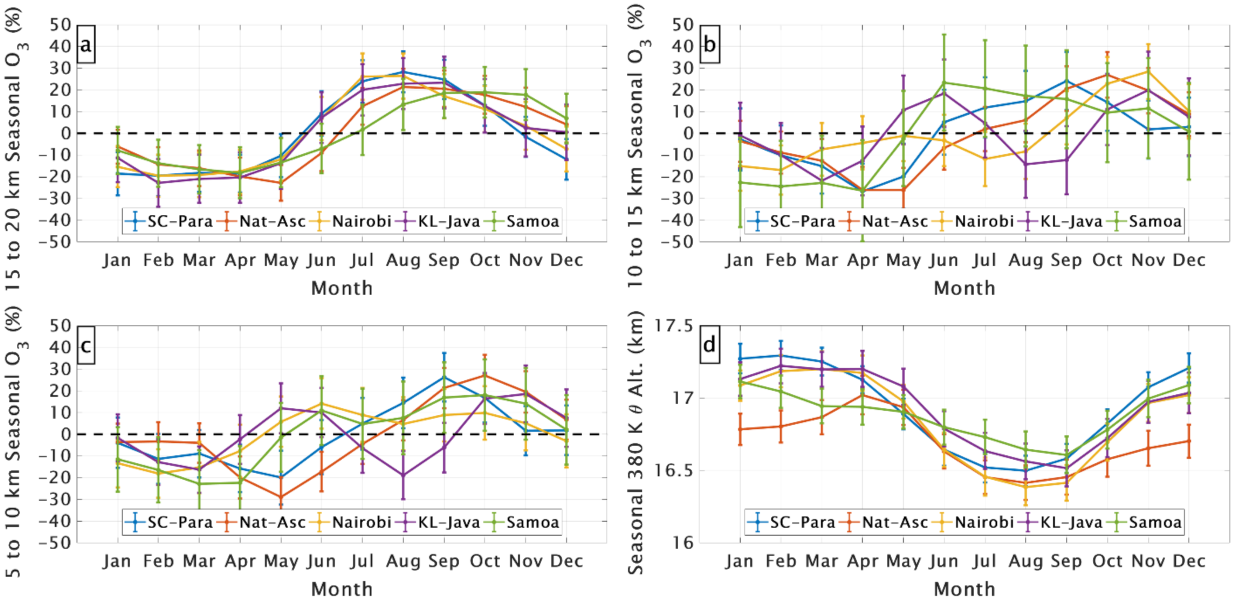


Figure 3. Seasonal ozone variability, expressed as percent anomaly from annual mean, from the MLR model in the LMS (a), FT (b and c). Tropopause Height (TH) is (d) based on the 380 K potential temperature surface from the radiosondes.

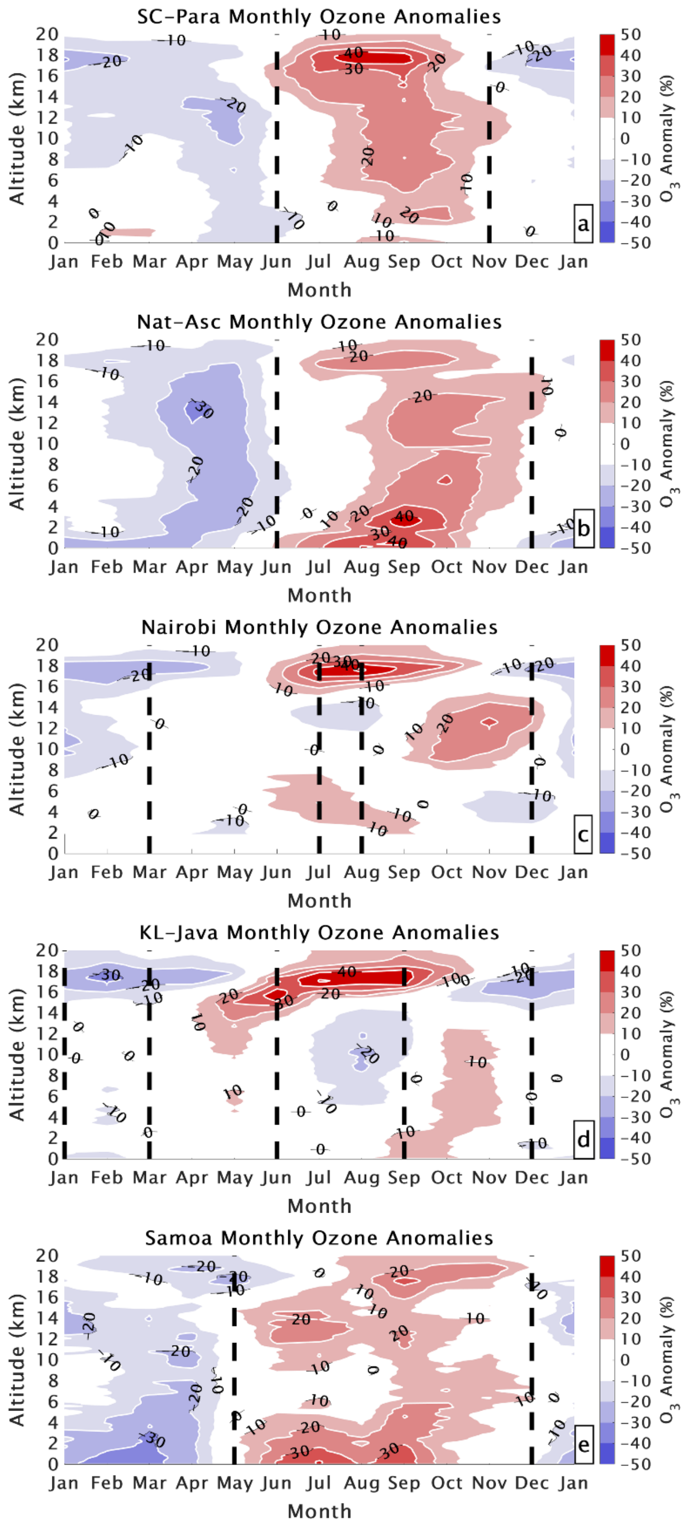


Figure 4. Monthly averaged $O_3$ mixing ratio anomalies in percent from the annual mean from the surface to 20 km altitude for the two individual and three combination sites. Black dashed lines (same as the white dashed lines in **Figure 2**) indicate transition periods marked by sign changes to the climatological FT and LMS $O_3$ amounts (see Section 3.1).

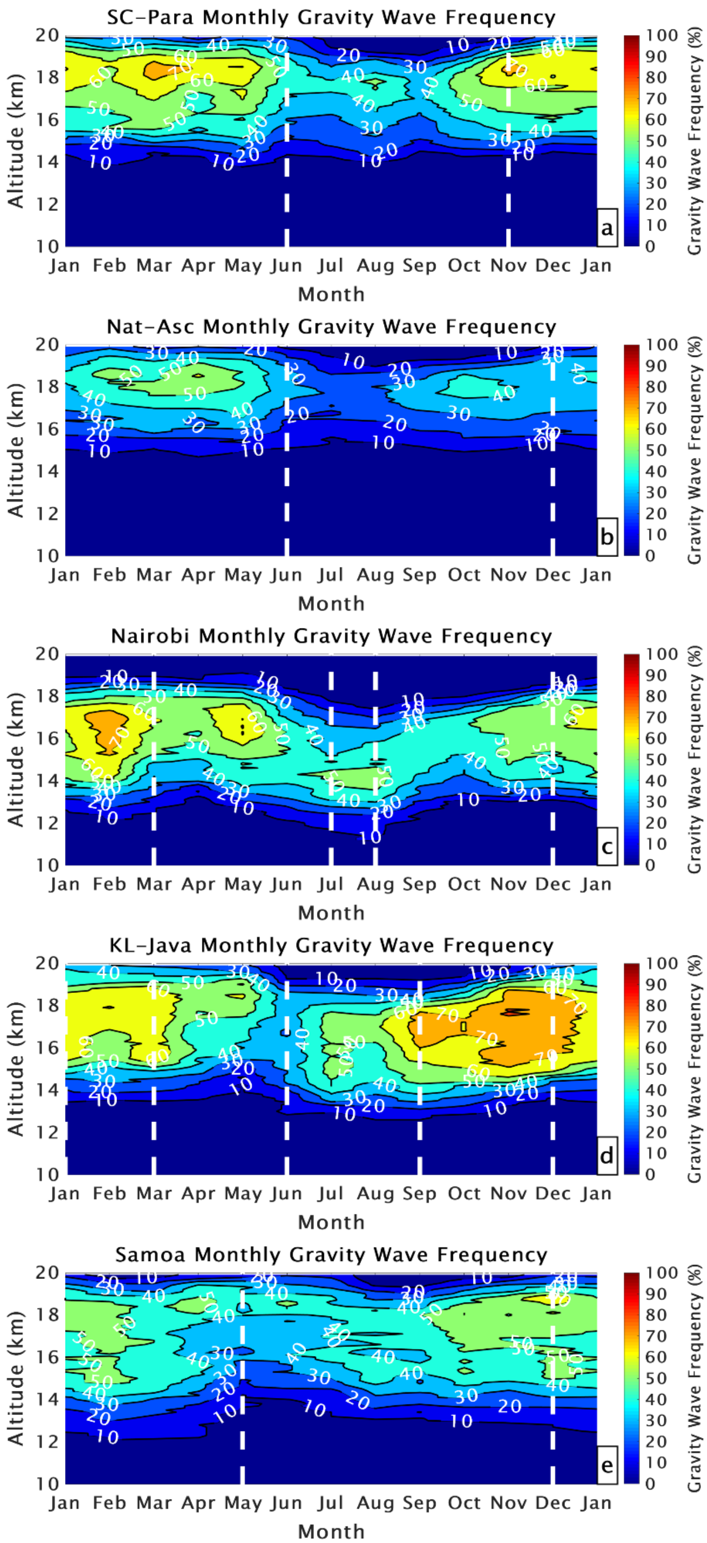


Figure 5. Monthly averaged gravity wave frequency (GWF) in percent from 10 to 20 km altitude corresponding to the profiles in Figure 2 for the two individual and three combination sites. White dashed lines are set by the ozone seasonal transitions as shown as in **Figures 2 and 4.**

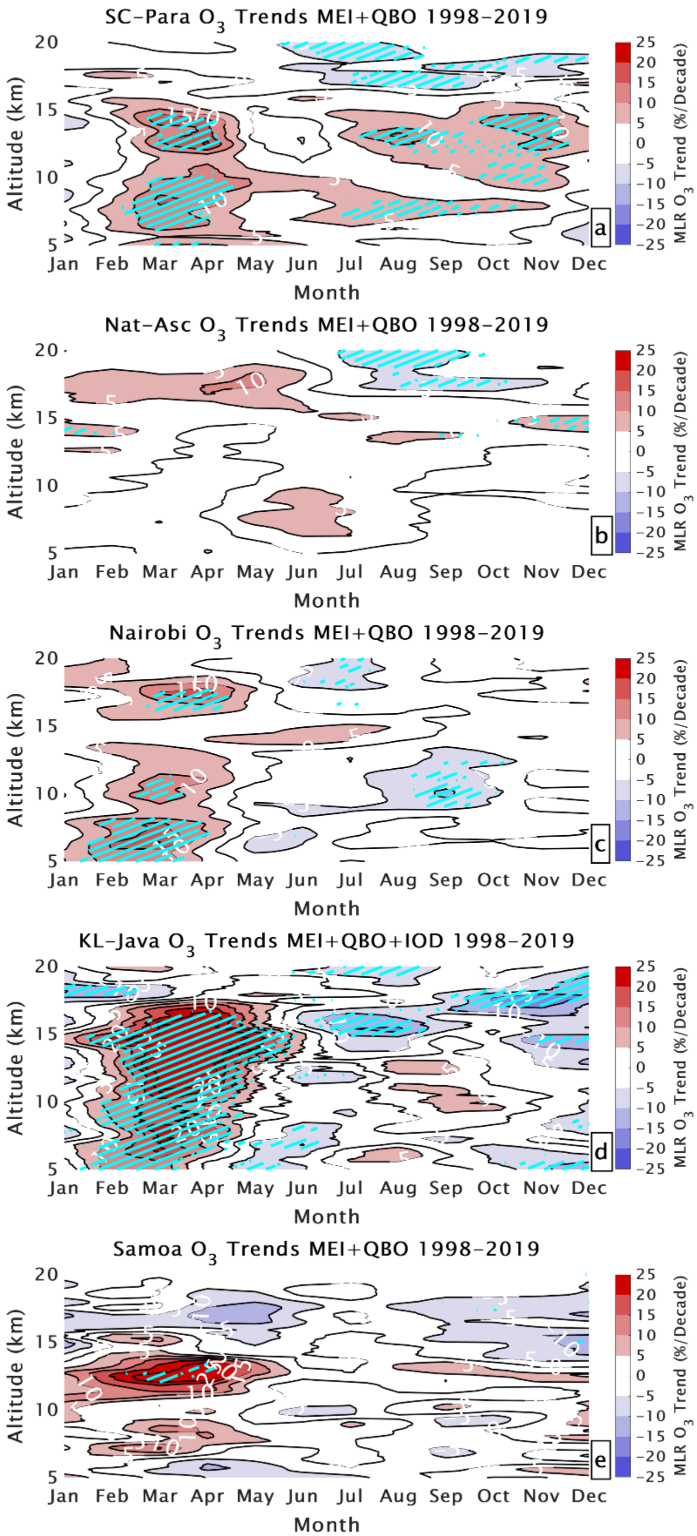


Figure 6. Monthly MLR ozone linear trends from 5 to 20 km in percent per decade for the two individual and three combination sites. Positive trends are shown in red and negative trends are shown in blue. Trends that are significant with 95% confidence shown with cyan hatching.

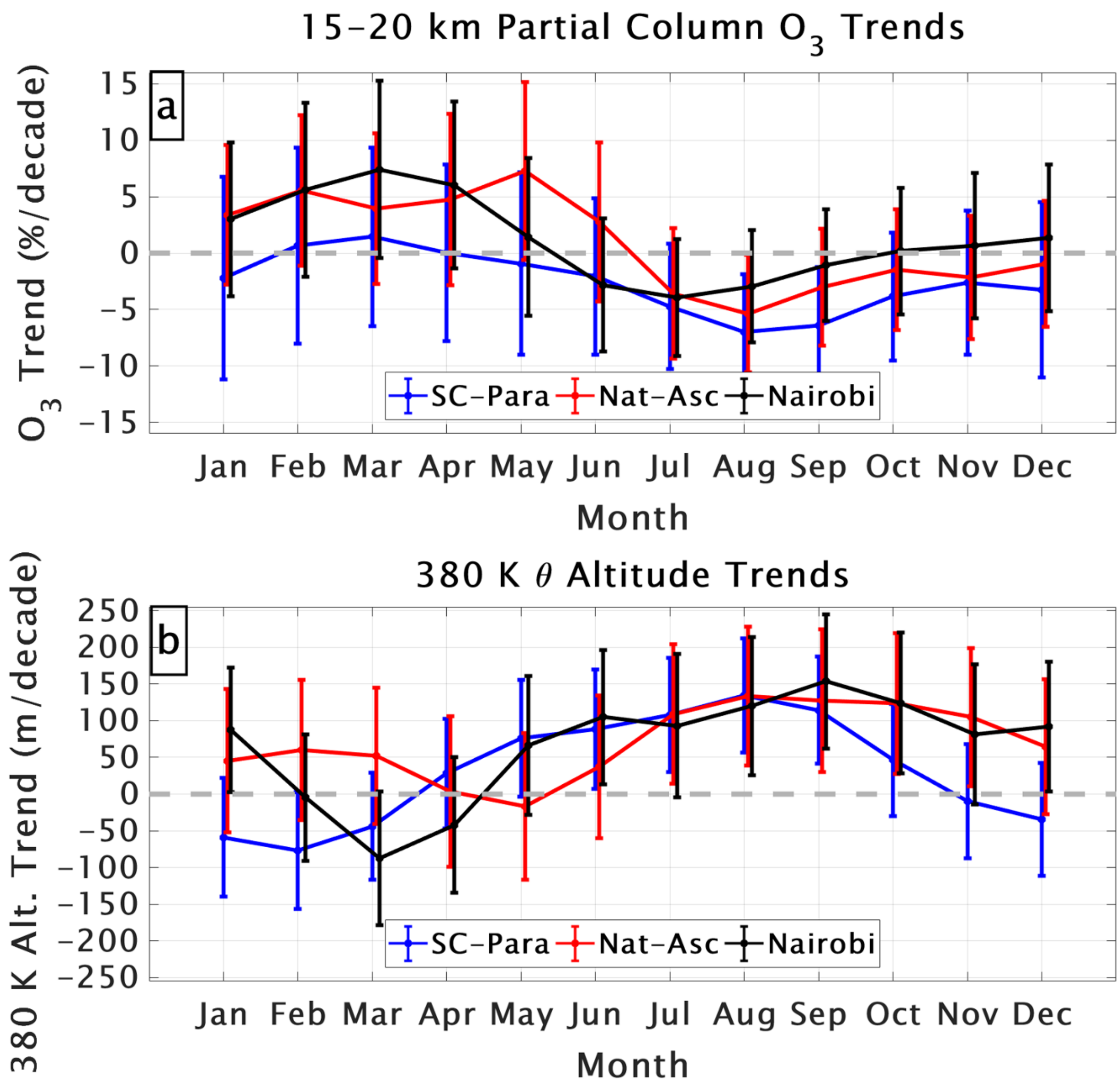


Figure 7. Monthly MLR trends in (a) LMS ozone column changes derived from SHADOZ sondes at the three indicated sites; (b) corresponding TH trends from the radiosondes. Dots represent the values and the error bars indicate the 95% confidence intervals.

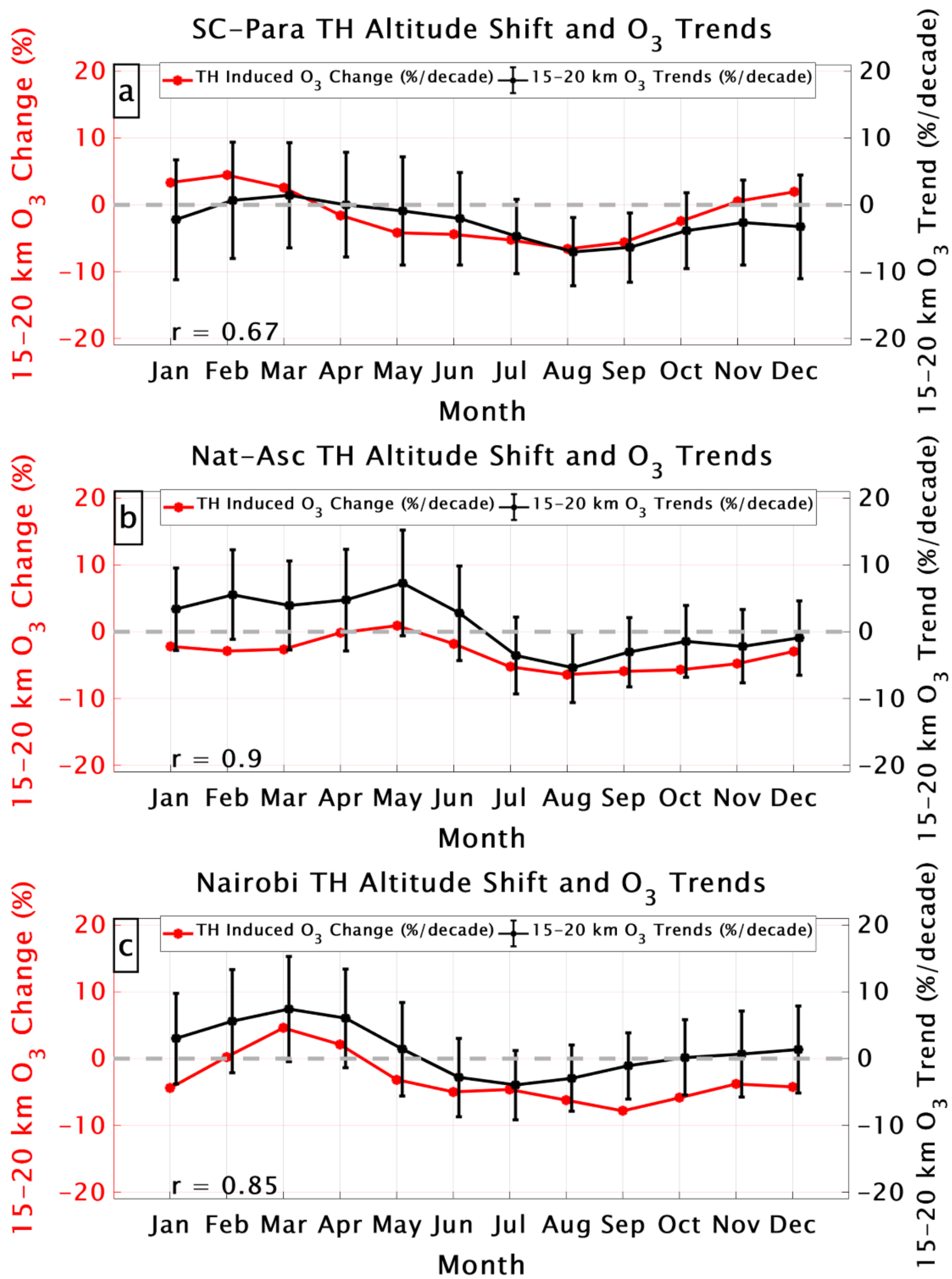


Figure 8. Monthly MLR LMS ozone trends and error bars in percent per decade (black), and LMS ozone change induced by shifting the MLR seasonal ozone profiles by the TH trend in m per decade (red). (a) SC-Para, (b) Nat-Asc, (c) Nairobi.

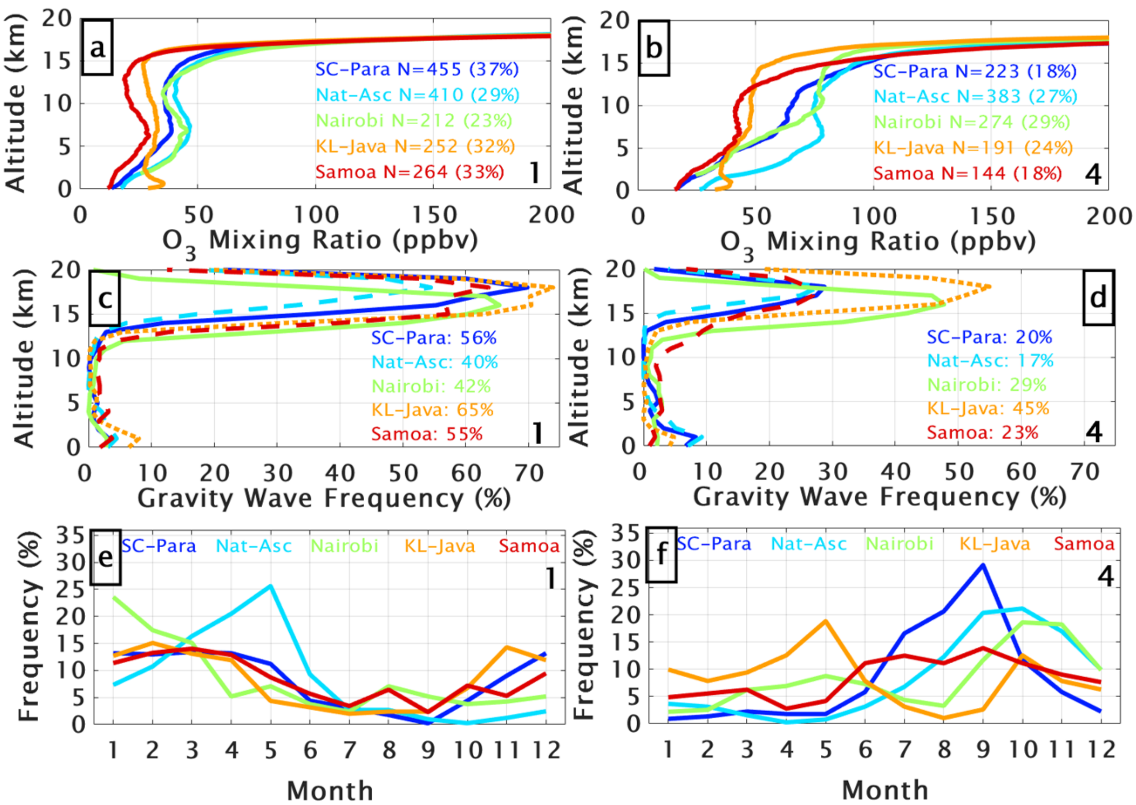


Figure 9. (a, b): SOM cluster ozone means for the two individual and three combination sites. The number and percentage of profiles contributing to each of four clusters (two not shown) appear in each frame. (c, d): Gravity wave frequency (GWF in text) as a function of altitude corresponding to SOM clusters 1 and 4. Average percentage GWF from 15 to 20 km (LMS) for each site is shown in the frames. (e, f) monthly frequency distribution for the profiles corresponding to the SOM clusters.

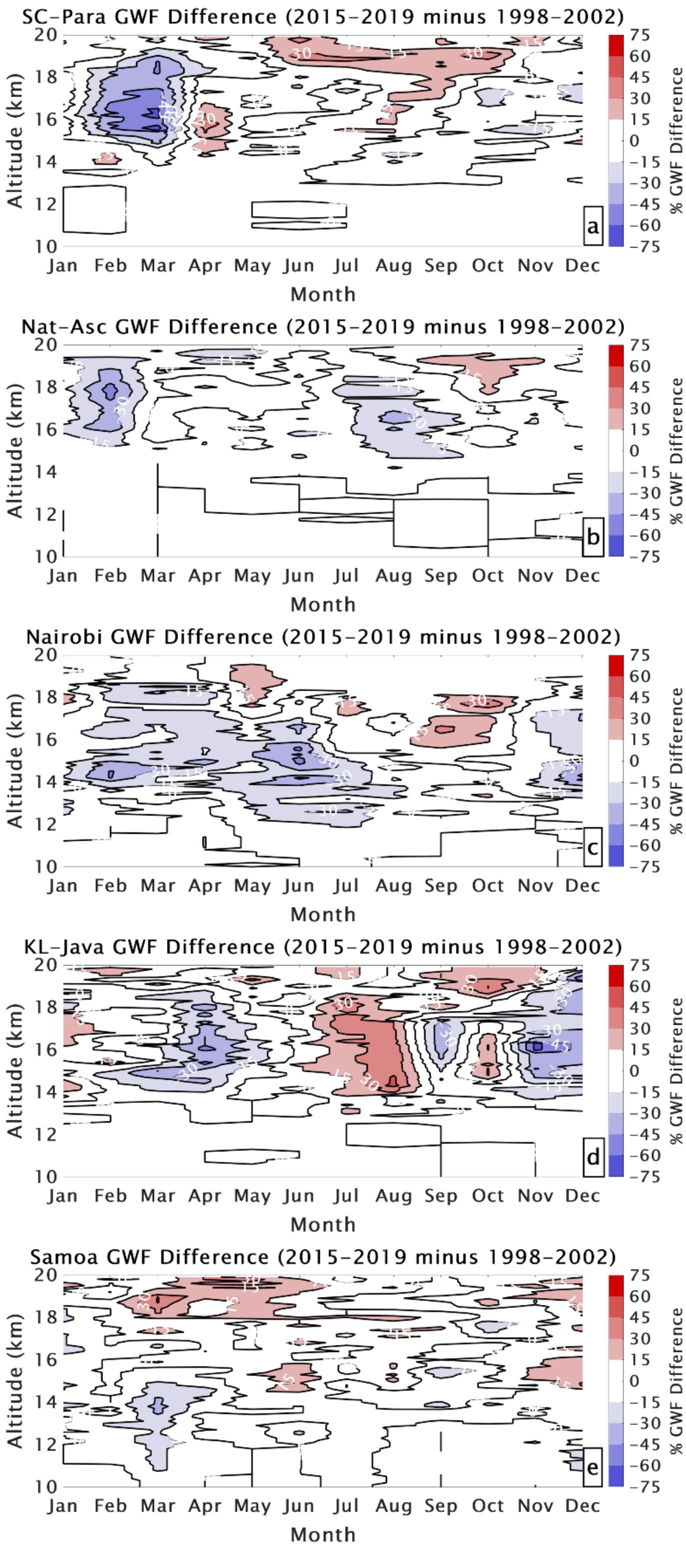


Figure 10. Change in monthly GWF over two periods (2015-2019 minus 1998-2002) from 10 to 20 km altitude. Increases in GWF are shown in red and decreases in GWF are shown in blue for the two individual and three combination sites.